

Switchable moiré potentials in ferroelectric WTe₂/WSe₂ superlattices

Kaifei Kang¹, Wenjin Zhao², Yihang Zeng³, Kenji Watanabe⁴, Takashi Taniguchi⁴, Jie Shan¹⁻³,
and Kin Fai Mak¹⁻³

¹School of Applied and Engineering Physics, Cornell University, Ithaca, NY, USA

²Kavli Institute at Cornell for Nanoscale Science, Ithaca, NY, USA

³Laboratory of Atomic and Solid State Physics, Ithaca, NY, USA

⁴National Institute for Materials Science, 1-1 Namiki, 305-0044 Tsukuba, Japan

Email: jie.shan@cornell.edu; kinfai.mak@cornell.edu

Moiré materials, with superlattice periodicity many times the atomic length scale, have enabled the studies of strong electronic correlations and band topology with unprecedented tunability¹⁻⁵. However, nonvolatile control of the moiré potentials, which could allow on-demand switching of the superlattice effects, has not been achieved to date. Here we demonstrate the switching of the correlated and moiré band insulating states and the associated nonlinear anomalous Hall effect by the ferroelectric effect. This is achieved in a ferroelectric WTe₂ bilayer of the T_d structure with a centered-rectangular moiré superlattice induced by interfacing with a WSe₂ monolayer of the H structure. The results can be understood in terms of polarization-dependent charge transfer between two WTe₂ monolayers, which possess very different moiré potential depths; ferroelectric switching thus turns on/off the superlattice. Our study demonstrates the potential of creating new functional moiré materials by incorporating intrinsic symmetry-breaking orders⁶⁻⁸.

Main

Two-dimensional ferroelectric materials have attracted much recent interest due to their potentials in non-volatile memory device applications⁹. In addition to intrinsic ferroelectric materials¹⁰⁻¹², such as CuInP₂S₆ and few-layer T_d-WTe₂, ferroelectricity has also been realized recently in moiré heterostructures¹³⁻¹⁷, enabling non-volatile control of correlated electronic states and superconductivity. However, non-volatile electrical switching of the moiré trapping potentials for electrons and the associated superlattice effects has not been realized to date. Here we achieve this goal by utilizing the intrinsic ferroelectricity in angle-aligned bilayer T_d-WTe₂/monolayer H-WSe₂ moiré heterostructures.

Monolayer WTe₂ of the T_d crystal structure consists of a layer of W atoms between two layers of Te atoms in the distorted octahedral coordination¹⁸. The structure is centrosymmetric with a mirror line along the crystal b-axis. At charge neutrality, the material is a quantum spin Hall insulator¹⁹⁻²¹. Bilayer T_d-WTe₂ is made of two antiparallel monolayers; the structure becomes non-centrosymmetric with a polar axis²² (inclined from the out-of-plane direction). The presence of the polar axis stabilizes ferroelectricity¹² and generates Berry curvature dipoles in the momentum space²³ responsible for the nonlinear anomalous Hall effect²⁴⁻²⁶. Bilayer T_d-WTe₂ is a topologically trivial insulator. Figure 1c illustrates its schematic band structure with a flat valence band centered at the Γ -point of the Brillouin zone and dispersive conduction bands away

from the Γ point^{27,28}. The bands are layer-polarized by the spontaneous out-of-plane electric polarization.

WTe₂/WSe₂ moiré superlattice

We introduce moiré potentials to bilayer WTe₂ by adding a WSe₂ monolayer on it (Fig. 1a). The WSe₂ monolayer is of the H crystal structure, in which the W atoms are between the Se atoms in the trigonal prismatic coordination. The zigzag or armchair crystal axis of WSe₂ is aligned to the crystal a-axis of WTe₂. A nearly centered-rectangular moiré superlattice is expected with periods 6.9 nm and 6.4 nm along the a- and b-axis of WTe₂, respectively. These values are estimated from the lattice mismatch between the two materials (5% and 9%) along the two axes. The corresponding moiré density, n_M , is about $4.5 \times 10^{12} \text{cm}^{-2}$. These estimates are in good agreement with the experimental moiré pattern of a typical aligned WTe₂/WSe₂ heterostructure obtained by piezoresponse force microscopy (Fig. 1b, see Methods and Extended Data Fig. 1 for details). The two lattice vectors form an angle of about 84 degrees. The moiré lattice is robust and insensitive to twist-angle variations in the sample as a result of the large lattice mismatch. The nearly centered-rectangular lattice also contrasts with the triangular and honeycomb moiré lattices examined by most of the existing studies to date¹⁻⁵.

The heterostructure has a type-I band alignment with both the conduction band minimum and valence band maximum from bilayer WTe₂ (Ref. ²⁹). The WSe₂ layer remains charge-neutral at all times; it only provides a moiré potential responsible for the flat bands in the WTe₂ layer. Moreover, the top WTe₂ layer directly interfacing with WSe₂ is expected to experience a substantially stronger moiré potential compared to the bottom WTe₂ layer; the moiré bands for the top layer are expected to be much flatter (Fig. 1c). Such layer-sensitive moiré effects in bilayer WTe₂, combined with its intrinsic ferroelectric order, form the basis for ferroelectric control of the moiré potential in this study.

Below we demonstrate the effects of ferroelectric switching on the correlated insulating states and the Berry curvature dipole distribution in the correlated flat bands. The heterostructure is encapsulated between top and bottom boron nitride and graphite gates for independent controls of the charge carrier density ν (in units of n_M) and the electric field E perpendicular to the sample plane (positive field defined as pointing from WTe₂ to WSe₂). See Methods for details on device fabrications, calibration of moiré density and measurements.

To contrast the behavior of bilayer WTe₂ devices, we first examine the density and electric field-dependent transport properties in an angle-aligned monolayer WTe₂/monolayer WSe₂ heterostructure (Fig. 1e). Since monolayer WTe₂ is a quantum spin Hall insulator¹⁹⁻²¹, we fabricate a Corbino geometry device in order to access the bulk resistivity of the material (Methods and Extended Data Fig. 2). Because the electrical contact resistance of this device increases substantially below 30 K, we limit our measurements down to 30 K. In Fig. 1e, we observe resistance peaks at filling factors of $\nu = 0, -1, -2$. They correspond to the band insulating state when WTe₂ is at charge neutrality ($\nu = 0$), the moiré band insulating state when the first moiré valence band is fully filled with holes ($\nu = -2$), and the correlated insulating state (likely a Mott insulator) for a half-filled moiré band ($\nu = -1$). The insulating states at $\nu = -1, -2$ confirms the formation of flat moiré valence bands in monolayer WTe₂. In contrast, no insulating state is observed at $\nu = 1, 2$ on the electron doping side (see also Fig. 2, 3). The result

demonstrates the negligible moiré effects on the conduction bands possibly due to the small conduction band mass in WTe_2 (Ref. ^{27,28}) and the small moiré periods in the $\text{WTe}_2/\text{WSe}_2$ heterostructure. Also, all of the observed insulating states show weak and non-hysteretic electric field dependence, consistent with the absence of ferroelectricity in monolayer WTe_2 (Ref. ¹²).

Switchable moiré potentials by ferroelectricity

Next we examine the density and electric field dependent resistance in a bilayer WTe_2 device under forward (from negative to positive) and backward (from positive to negative) scans of the electric field in Fig. 2a and 2b, respectively. The Corbino geometry is no longer needed because bilayer WTe_2 is a topologically trivial insulator ^{27,28}. The electrical contacts are also better than the monolayer device; lower temperature measurements are possible. Similar to the monolayer device, we observe insulating states at $\nu = -1, -2$ for hole doping, a charge-neutral insulating state at $\nu = 0$ and no moiré insulating states for electron doping. Unlike the monolayer device, strong electric field dependence is observed. In particular, robust insulating states at $\nu = -1, -2$ are observed mostly for $E \lesssim 0.3$ V/nm in the forward scan (Fig. 2a) and for $E \lesssim 0.1$ V/nm in the backward scan (Fig. 2b). A sharp resistance jump and an electric field hysteresis are also observed near these critical fields, as exemplified by the electric field dependent resistance at $\nu = -1$ in Fig. 2c (similar data at other filling factors are shown in Extended Data Fig. 3). In addition to the hysteresis, a non-monotonic electric field dependence is also observed (the origin is discussed in Methods). The results clearly demonstrate the effects of ferroelectric switching (in bilayer WTe_2) on the moiré physics. The center of the ferroelectric switching is shifted from 0 V/nm to ~ 0.2 V/nm and disperses with hole doping because of the built-in electric field in the asymmetric heterostructure (WSe_2 is on top of WTe_2).

We further illustrate the effects of ferroelectric switching by plotting the density dependent resistance near the center of the hysteresis (at fixed $E = 0.2$ V/nm) for both forward and backward field scans (Fig. 2d). The two cases represent the two remnant states of spontaneous polarization P in the ferroelectric WTe_2 : positive polarization ($P > 0$, pointing from WTe_2 to WSe_2) for backward scan and negative polarization ($P < 0$, pointing from WSe_2 to WTe_2) for forward scan. Insulating states at $\nu = -1, -2$ associated with the moiré valence band are observed only for $P < 0$; only the $\nu = 0$ insulating state remains for $P > 0$. An on-off ratio of ~ 10 for the insulating states at $\nu = -1, -2$ is achieved upon ferroelectric switching (inset).

The results above can be understood based on the interlayer transfer of mobile holes in bilayer WTe_2 driven by its spontaneous ferroelectric polarization, which originates from the electric-field-switchable ionic displacements in the material ³⁰. When positive polarization ($P > 0$) is prepared, the internal electric field from the displaced ions (or bound charges) within the bilayer WTe_2 is negative; the field splits the electronic bands of the top and bottom WTe_2 layer via the Stark effect and pushes the mobile holes to the bottom layer (Fig. 1d). The reverse happens when negative polarization ($P < 0$) is prepared (Fig. 1d). Because holes in the top layer interfacing directly with the WSe_2 layer experience a strong moiré potential, robust insulating states at $\nu = -1, -2$ are observed for $P < 0$. The absence of these insulating states for $P > 0$ shows the negligible moiré potential in the bottom WTe_2 layer.

Note that the total electric polarization is a sum of both the bound charge and mobile hole contributions; the two contributions point in opposite directions. The bound charge contribution

dominates over the entire hole doping range; this guarantees nearly complete (i.e. 100 %) interlayer hole transfer upon ferroelectric switching and the emergence of the moiré insulating states at $\nu = -1, -2$ for $P < 0$. Otherwise, the more mobile holes in the bottom layer would electrically short the bilayer conduction irrespective of the sign of P ; moiré insulating states would not have been observed.

Variable-range hopping transport

To gain further insights into how ferroelectric switching influences the charge transport in bilayer WTe_2 , we perform temperature dependence studies for both $P < 0$ and $P > 0$, which correspond to with and without moiré effects, respectively. Figure 3a and 3b show the density dependent resistance at varying temperatures (5 – 90 K) for the two states. Metallic transport (decreasing resistance with decreasing temperature) is observed only on the electron doping side, where moiré physics is not observable; a metal-insulator transition is also observed near $\nu = 0.7$. For the entire hole doping range, the material exhibits insulator-like behavior (increasing resistance with decreasing temperature) even when there is no moiré physics for $P > 0$. The $\nu = -1, -2$ insulating states for $P < 0$ survive up to about 70 K.

The temperature dependent resistance at $\nu = -1$ for both $P < 0$ and $P > 0$ is shown in Fig. 3c (similar dependence at other densities is shown in Extended Data Fig. 4). For temperatures below about 100 K, the resistance R scales with the temperature T according to the Efros-Shklovskii variable-range hopping model^{31,32}, $R \propto \exp(T_0/T)^{1/2}$, for over two orders of magnitude in R .

The characteristic temperature $T_0 = \frac{2.8 e^2}{4\pi\epsilon\epsilon_0 k_B \xi}$ is inversely proportional to the localization length ξ of holes in the bilayer WTe_2 (here e , ϵ_0 , ϵ and k_B denote the electron charge, the vacuum permittivity, the dielectric constant of the substrate and the Boltzmann constant, respectively). The density dependence of T_0 is extracted in Fig. 3d. The temperature T_0 is substantially enhanced over the entire hole doping range for $P < 0$; additional enhancement at the $\nu = -1, -2$ insulating states is also observed. The results demonstrate the additional localization of holes that shortens ξ (≈ 35 nm for $T_0 = 300$ K) when the moiré potential is turned on for $P < 0$.

Nonlinear anomalous Hall effect

Finally, we examine the effects of ferroelectric switching on the topological transport properties. The presence of an in-plane polar axis (along the mirror line of WTe_2) in the non-centrosymmetric centered-rectangular moiré lattice allows the generation of an out-of-plane magnetization under a bias current perpendicular to the mirror line^{23,25}. The current-induced magnetization can in turn induce an anomalous Hall effect probed by the same bias current. The anomalous Hall voltage thus scales with the bias current squared, giving rise to a nonlinear anomalous Hall effect (NAHE)²³⁻²⁶. The effect provides a powerful probe of the Berry curvature dipoles (an imbalance in the Berry curvature occupations) in moiré materials^{33,34}.

To measure the NAHE in the $\text{WTe}_2/\text{WSe}_2$ moiré heterostructure, we bias an ac current (I) perpendicular to the mirror line of the moiré lattice and simultaneously measure the first-harmonic longitudinal voltage (V_{\parallel}) and the second-harmonic transverse voltage ($V_{\perp}^{2\omega}$) (Methods). Figure 4a and 4b show the density and electric field dependence of $V_{\perp}^{2\omega}/I^2$ under forward and backward scans in the electric field, respectively. The quantity provides a measure of the nonlinear anomalous Hall response (Extended Data Fig. 5). The measurement temperature is

kept above 25 K for good electrical contacts. The results are correlated with the behavior for the resistance in Fig. 2b and 2c. In particular, strong NAHE with sign reversal in $V_{\perp}^{2\omega}/I^2$ is observed at $\nu = -1, -2$ mainly for $E \lesssim 0.3$ V/nm in the forward scan and for $E \lesssim 0.1$ V/nm in the backward scan; or else only the $\nu = 0$ region shows strong NAHE; there is also a sharp jump in $V_{\perp}^{2\omega}/I^2$ and an electric field hysteresis near these critical electric fields. We extract the density dependent $V_{\perp}^{2\omega}/I^2$ for the two remnant states of spontaneous polarization $P < 0$ and $P > 0$ in Fig. 4c. (Temperature dependence is shown in Extended Data Fig. 6.) Strong NAHE with sign reversal in $V_{\perp}^{2\omega}/I^2$ is observed at $\nu = 0, -1, -2$ for $P < 0$; only the characteristic response at $\nu = 0$ remains for $P > 0$.

The results demonstrate the ferroelectric switching of the NAHE. In the absence of the moiré potential ($P > 0$), the Berry curvature and its dipole are concentrated near the WTe_2 conduction and valence band edges; the NAHE is strong near charge neutrality ($\nu = 0$); the sign reversal in $V_{\perp}^{2\omega}/I^2$ reflects the opposite Berry curvature dipoles for the conduction and valence bands^{24,27}. When flat bands are formed due to the moiré potential ($P < 0$), the Berry curvature and its dipole are redistributed within the moiré Brillouin zone³⁵; the small moiré band gap is expected to greatly enhance the Berry curvature effects^{35,36}. In the strong correlation limit (Coulomb repulsion exceeds the electronic bandwidth), Hubbard bands are formed; Berry curvatures of opposite signs are expected to concentrate near the Hubbard band edges, resulting in the characteristic NAHE response observed at $\nu = -1, -2$. Interestingly, the sign reversal in $V_{\perp}^{2\omega}/I^2$ at $\nu = -1, -2$ resembles the resets of the Hall density at integer fillings in graphene moiré materials³⁷. The resets reflect the changing carrier type upon doping an insulating state.

Conclusions

In conclusion, we have demonstrated electrical switching of the moiré potential by ferroelectricity in angle-aligned bilayer WTe_2 /monolayer WSe_2 ; the heterostructure forms a centered-rectangular moiré lattice. The emergence of moiré insulating states at integer filling factors is fully controlled by the spontaneous polarization direction. Ferroelectric switching can also redistribute the Berry curvature dipole in the momentum space, giving rise to a strong and sign-reversed NAHE at integer fillings when the moiré potential is turned on. Although the experimental results can be qualitatively understood based on the formation of Hubbard bands, the distribution of Berry curvature dipole within the Hubbard bands in the strong correlation limit (versus that within the single-particle moiré bands in the non-interacting limit) is an open question for future studies; understanding the NAHE in the hopping transport regime³⁸ (Fig. 3 and Extended Data Fig. 6) also requires further investigations.

Methods

Device fabrication

T_d - WTe_2 /H- WSe_2 moiré heterostructures were fabricated using the standard layer-by-layer stacking method³⁹. In short, air-sensitive monolayer and bilayer WTe_2 flakes were exfoliated and identified based on their optical contrast on Si substrates inside a nitrogen-filled glovebox. The a- and b-axis of the WTe_2 flakes were determined according to the sharp sample edges. Monolayer WSe_2 flakes were exfoliated under ambient conditions. The WSe_2 crystal axes were determined by polarization- and angle-resolved second-harmonic generation spectroscopy⁴⁰. The zigzag or armchair axis of WSe_2 was aligned to the crystal a-axis of WTe_2 during the stacking

process. To complete the devices, we first defined platinum electrodes in the Hall-bar geometry on a hexagonal boron nitride (hBN)/graphite heterostructure (that serves as a bottom gate) using electron-beam lithography. We then used a polymer stamp consisting of a polycarbonate (PC) film on polydimethylsiloxane (PDMS) to sequentially pick up flakes of graphite, hBN, a WSe₂ monolayer, and a WTe₂ monolayer or bilayer. The finished heterostructure on the stamp was released onto the pre-patterned platinum electrodes at 180°C. The polymer stamp was then dissolved in chloroform. To fabricate Corbino geometry devices, we further inserted a thin hBN spacer between the moiré heterostructure and the platinum electrodes so that the WTe₂ sample edges do not touch the metal electrodes^{41,42}. See Extended Data Fig. 2 for the device geometry.

Linear and nonlinear electrical measurements

Electrical transport measurements were carried out in an Oxford Teslatron cryostat down to 1.8 K. Both linear and nonlinear electrical measurements were performed using the standard lock-in technique. Specifically, current with constant amplitude of 0.5 μ A and modulation frequency of 17 Hz was biased along the crystal a-axis of WTe₂. The longitudinal voltage drop at the same frequency (V_{\parallel}) and the Hall voltage drop at the second-harmonic frequency ($V_{\perp}^{2\omega}$) were simultaneously recorded by lock-in amplifiers (Stanford Research SR830). In general, the contact resistance increases substantially at low temperatures; we therefore limited the nonlinear anomalous Hall measurements to temperatures above 25 K. The nonlinear anomalous Hall response was verified to be independent of the excitation frequency (Extended Data Fig. 5). In addition, we also measured the longitudinal resistance with current biased along the crystal b-axis of WTe₂ (Extended Data Fig. 7). The linear transport behavior is largely independent of the bias current direction.

The carrier density (n) and moiré density (n_M) of the device shown in the main text were calibrated using the parallel-plate capacitor model: $n = \frac{\epsilon\epsilon_0 V_{tg}}{d_{tg}} + \frac{\epsilon\epsilon_0 V_{bg}}{d_{bg}}$. Here $d_{tg} \approx 4$ nm and $d_{bg} \approx 22$ nm are the top and bottom hBN gate dielectric thicknesses measured by atomic force microscopy (AFM); V_{tg} and V_{bg} are the top and bottom gate voltages; ϵ_0 is the vacuum permittivity; and $\epsilon \approx 3$ is the hBN dielectric constant. A hole density of $(5.0 - 5.5) \times 10^{12}$ cm⁻² at $\nu = -1$ was obtained using the applied gate voltages relative to those at $\nu = 0$; the value is about 10-20 % larger than the moiré density (4.5×10^{12} cm⁻²) estimated using the known lattice parameters (see main text). The discrepancy may arise from misalignment of the WTe₂ and WSe₂ crystal axes (up to about 2 degrees) as well as identification of the gate voltage corresponding to zero doping density.

Piezoresponse force microscopy (PFM)

To characterize the moiré pattern using PFM, we fabricated an angle-aligned monolayer T_d-WTe₂/H-WSe₂ heterostructure on a polymer stamp consisting of PC on PDMS. Flakes of hBN, monolayer WTe₂ and monolayer WSe₂ were sequentially picked up by the polymer stamp. We then flipped the stamp for the PFM characterization with WSe₂ on the top surface to protect WTe₂ from oxidation. PFM was performed using a Bruker Veeco Icon AFM with Oxford Instrument Asylum Research ASYELEC-01 Ti/Ir coated silicon probes. An ac bias voltage with magnitude of 4 V and frequency of 680 kHz was applied to drive the probe during the scan. To improve the signal-to-noise ratio of the obtained moiré pattern, the raw PFM images were Fourier filtered with a threshold of 72% of the maximum intensity (Extended Data Fig. 1).

Non-monotonic electric-field dependent resistance

Extended Data Fig. 3 shows the electric-field dependent longitudinal resistance for both field scan directions at selected filling factors. We focus our discussions on $\nu = 0$ and 1, at which high out-of-plane electric fields can be applied. Non-monotonic electric field dependence of the resistance is observed. In particular, resistance peaks are observed at electric fields $E \approx -0.3$ V/nm and 0.55 V/nm for $\nu = 0$ and at $E \approx 0.1$ V/nm and 0.65 V/nm for $\nu = 1$.

To understand the observation, we consider the band structure of and the interlayer charge distribution in bilayer WTe_2 under an applied electric field E . In the presence of a spontaneous polarization P (dominated by the bound charge contribution), the total electric field is given by $E_{tot} = E - P/\chi\epsilon_0$ (χ and ϵ_0 denote the electric susceptibility and the vacuum permittivity, respectively). At $\nu = 0$ (charge neutrality), the resistance reflects the charge gap size of bilayer WTe_2 . The gap size is the largest for $E_{tot} = 0$ and decreases linearly with E_{tot} due to the interlayer Stark effect²⁷ (Fig. 1c). The maximum gap size is therefore expected at $E = \pm|P|/\chi\epsilon_0$, which is consistent with the observed resistance peaks at $E \approx -0.3$ V/nm and 0.55 V/nm in Extended Data Fig. 3. The asymmetry in the observed electric fields is caused by the heterostructure asymmetry, which shifts the center of the electric-field dependence by about 0.2 V/nm. Away from these two fields, the gap size decreases with E_{tot} , and the resistance decreases.

On the other hand, the resistance at $\nu = 1$ is largely determined by the location of the doped holes, specifically, high (low) resistance for holes residing in the top (bottom) WTe_2 layer. For $P < 0$, a negative electric field ($E < 0$) pushes the doped holes away from the $\text{WSe}_2/\text{WTe}_2$ interface, thus reducing the moiré effects (Fig. 1d); the resistance decreases monotonically (Extended Data Fig. 3). For $P > 0$, an electric field $E > 0.4$ V/nm pushes the doped holes towards the $\text{WSe}_2/\text{WTe}_2$ interface, therefore enhancing the moiré effects (Fig. 1d); the resistance increases and peaks at $E \approx 0.65$ V/nm, beyond which the charge gap decreases due to the interlayer Stark effect (as discussed above). Finally, hysteretic switching behavior is observed for $0 < E < 0.4$ V/nm; the resistance is dependent on the direction of P . The center of the ferroelectric switching is shifted by about 0.2 V/nm because of the heterostructure asymmetry.

Acknowledgements

We thank Angel Rubio, Yang Zhang and Jin Zhang for fruitful discussions.

Author contributions

K.K. fabricated the devices. K.K. and W.Z. performed the electrical measurements. Y.Z. and K.K. performed the PFM measurements. K.K. analyzed the data. K.W. and T.T. grew the hBN crystals. K.K., J.S. and K.F.M. designed the scientific objectives, oversaw the project, and co-wrote the manuscript. All authors discussed the results and commented on the manuscript.

References

1. Andrei, E.Y. & MacDonald, A.H. Graphene bilayers with a twist. *Nat. Mater.* **19**, 1265-1275 (2020).
2. Balents, L., Dean, C.R., Efetov, D.K. & Young, A.F. Superconductivity and strong correlations in moiré flat bands. *Nat. Phys.* **16**, 725-733 (2020).
3. Mak, K.F. & Shan, J. Semiconductor moiré materials. *Nat. Nanotechnol.* **17**, 686-695 (2022).
4. Kennes, D.M., *et al.* Moiré heterostructures as a condensed-matter quantum simulator. *Nat. Phys.* **17**, 155-163 (2021).
5. Andrei, E.Y., *et al.* The marvels of moiré materials. *Nat. Rev. Mater.* **6**, 201-206 (2021).
6. Xu, Y., *et al.* Coexisting ferromagnetic-antiferromagnetic state in twisted bilayer CrI₃. *Nat. Nanotechnol.* **17**, 143-147 (2022).
7. Song, T.C., *et al.* Direct visualization of magnetic domains and moiré magnetism in twisted 2D magnets. *Science* **374**, 1140 (2021).
8. Xie, H.C., *et al.* Twist engineering of the two-dimensional magnetism in double bilayer chromium triiodide homostructures. *Nat. Phys.* **18**, 30 (2022).
9. Qi, L., Ruan, S.C. & Zeng, Y.J. Review on Recent Developments in 2D Ferroelectrics: Theories and Applications. *Adv. Mater.* **33**, 2005098 (2021).
10. Chang, K., *et al.* Discovery of robust in-plane ferroelectricity in atomic-thick SnTe. *Science* **353**, 274-278 (2016).
11. Liu, F.C., *et al.* Room-temperature ferroelectricity in CuInP₂S₆ ultrathin flakes. *Nat. Commun.* **7**, 12357 (2016).
12. Fei, Z.Y., *et al.* Ferroelectric switching of a two-dimensional metal. *Nature* **560**, 336 (2018).
13. Zheng, Z., *et al.* Unconventional ferroelectricity in moiré heterostructures. *Nature* **588**, 71-76 (2020).
14. Yasuda, K., Wang, X.R., Watanabe, K., Taniguchi, T. & Jarillo-Herrero, P. Stacking-engineered ferroelectricity in bilayer boron nitride. *Science* **372**, 1458 (2021).
15. Wang, X.R., *et al.* Interfacial ferroelectricity in rhombohedral-stacked bilayer transition metal dichalcogenides. *Nat. Nanotechnol.* **17**, 367 (2022).
16. Weston, A., *et al.* Interfacial ferroelectricity in marginally twisted 2D semiconductors. *Nat. Nanotechnol.* **17**, 390 (2022).
17. Stern, M.V., *et al.* Interfacial ferroelectricity by van der Waals sliding. *Science* **372**, 1462 (2021).
18. Brown, B.E. Crystal Structures of WTe₂ and High-Temperature MoTe₂. *Acta Crystallogr.* **20**, 268 (1966).
19. Fei, Z.Y., *et al.* Edge conduction in monolayer WTe₂. *Nat. Phys.* **13**, 677 (2017).
20. Wu, S.F., *et al.* Observation of the quantum spin Hall effect up to 100 kelvin in a monolayer crystal. *Science* **359**, 76-79 (2018).
21. Zhao, W.J., *et al.* Determination of the Spin Axis in Quantum Spin Hall Insulator Candidate Monolayer WTe₂. *Phys. Rev. X* **11**, 041034 (2021).
22. Sakai, H., *et al.* Critical enhancement of thermopower in a chemically tuned polar semimetal MoTe₂. *Sci. Adv.* **2**, 1601378 (2016).
23. Sodemann, I. & Fu, L. Quantum Nonlinear Hall Effect Induced by Berry Curvature Dipole in Time-Reversal Invariant Materials. *Phys. Rev. Lett.* **115**, 216806 (2015).

24. Ma, Q., *et al.* Observation of the nonlinear Hall effect under time-reversal-symmetric conditions. *Nature* **565**, 337 (2019).
25. Kang, K.F., Li, T.X., Sohn, E., Shan, J. & Mak, K.F. Nonlinear anomalous Hall effect in few-layer WTe₂. *Nat. Mater.* **18**, 324 (2019).
26. Du, Z.Z., Lu, H.Z. & Xie, X.C. Nonlinear Hall effects. *Nat. Rev. Phys.* **3**, 744-752 (2021).
27. Xu, S.Y., *et al.* Electrically switchable Berry curvature dipole in the monolayer topological insulator WTe₂. *Nat. Phys.* **14**, 900 (2018).
28. Qian, X.F., Liu, J.W., Fu, L. & Li, J. Quantum spin Hall effect in two-dimensional transition metal dichalcogenides. *Science* **346**, 1344-1347 (2014).
29. Liu, Y.Y., Stradins, P. & Wei, S.H. Van der Waals metal-semiconductor junction: Weak Fermi level pinning enables effective tuning of Schottky barrier. *Sci. Adv.* **2**, 4(2016).
30. Wang, H. & Qian, X.F. Ferroelectric nonlinear anomalous Hall effect in few-layer WTe₂. *Npj Comput. Mater.* **5**, 119 (2019).
31. Efros, A.L., Nguyen, V. L., & Shklovskii, B.I. Variable Range Hopping in Doped Crystalline Semiconductors. *Solid State Commun.* **32**, 851-854 (1979).
32. Efros, A.L. & Shklovskii, B.I. Coulomb Gap and Low-Temperature Conductivity of Disordered Systems. *J. Phys. C Solid State* **8**, 49-51 (1975).
33. Sinha, S., *et al.* Berry curvature dipole senses topological transition in a moiré superlattice. *Nat. Phys.* **18**, 765 (2022).
34. He, P., *et al.* Graphene moiré superlattices with giant quantum nonlinearity of chiral Bloch electrons. *Nat. Nanotechnol.* **17**, 378 (2022).
35. Zhang, C.P., *et al.* Giant nonlinear Hall effect in strained twisted bilayer graphene. *Phys. Rev. B* **106**, 041111 (2022).
36. Xiao, D., Chang, M.C. & Niu, Q. Berry phase effects on electronic properties. *Rev. Mod. Phys.* **82**, 1959-2007 (2010).
37. Saito, Y., *et al.* Isospin Pomeranchuk effect in twisted bilayer graphene. *Nature* **592**, 220 (2021).
38. Burkov, A.A. & Balents, L. Anomalous Hall effect in ferromagnetic semiconductors in the hopping transport regime. *Phys. Rev. Lett.* **91**, 057202 (2003).
39. Wang, L., *et al.* One-Dimensional Electrical Contact to a Two-Dimensional Material. *Science* **342**, 614-617 (2013).
40. Tang, Y.H., *et al.* Simulation of Hubbard model physics in WSe₂/WS₂ moiré superlattices. *Nature* **579**, 353 (2020).
41. Zhu, J.C., Li, T.X., Young, A.F., Shan, J. & Mak, K.F. Quantum Oscillations in Two-Dimensional Insulators Induced by Graphite Gates. *Phys. Rev. Lett.* **127**, 247702 (2021).
42. Wang, P.J., *et al.* Landau quantization and highly mobile fermions in an insulator. *Nature* **589**, 225 (2021).

Figures

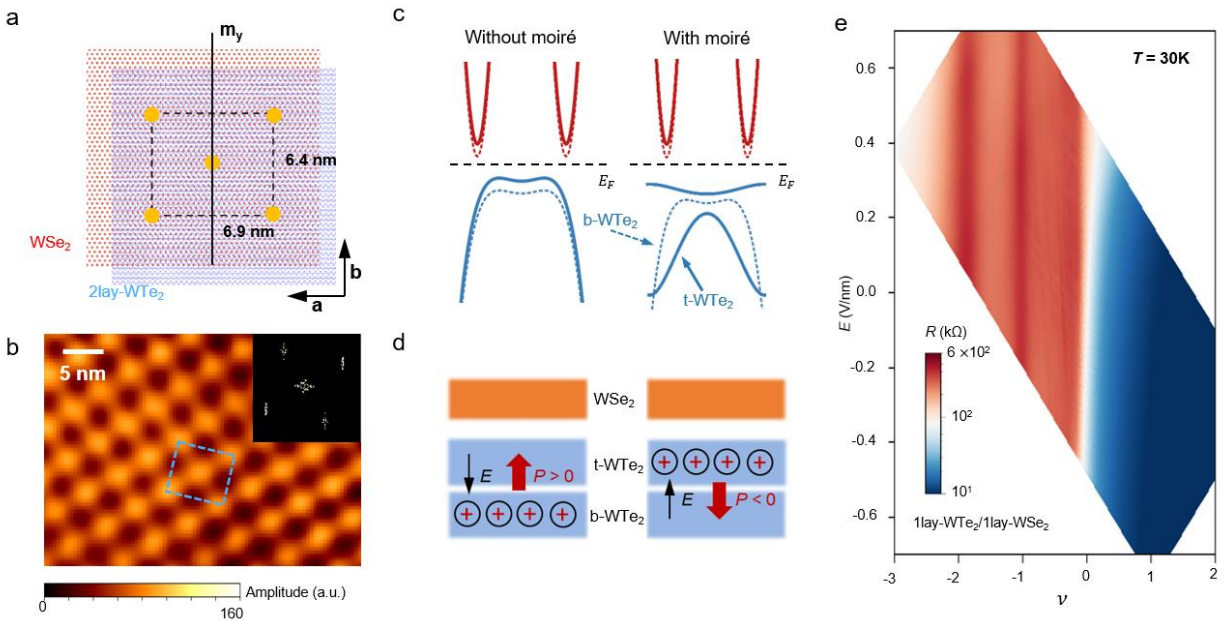


Figure 1 | Bilayer T_d -WTe₂/monolayer H-WSe₂ moiré heterostructure. **a**, Moiré superlattice for angle-aligned bilayer T_d -WTe₂/monolayer H-WSe₂ heterostructure. Only the W atoms are shown. Yellow dots denote the high-symmetry MM (W on W) sites, which form a centered-rectangular lattice with lattice constants of 6.9 nm along the crystal a-axis of WTe₂ and 6.4 nm along the crystal b-axis of WTe₂ (the mirror line m_y). The dashed rectangle marks the moiré unit cell. The black arrows mark the crystal a and b axes of bilayer WTe₂. **b**, PFM image of a typical moiré heterostructure. The dashed rectangle marks the moiré unit cell. Inset shows the Fourier transform of the PFM image. **c**, Schematics for the bilayer WTe₂ band structure with (right) and without (left) moiré effects. Red and blue colors correspond to conduction and valence bands, respectively. Right: moiré bands are formed on the top WTe₂ (t-WTe₂) layer only (solid blue curves). The bottom WTe₂ (b-WTe₂) layer experiences negligible moiré potential; no flat bands are formed (dashed lines). The horizontal black dashed line denotes the Fermi level. **d**, Polarization-dependent hole (red cross) distributions in bilayer WTe₂. P and E are, respectively, the spontaneous polarization and its corresponding internal electric field. **e**, Electric field and filling factor dependence for the longitudinal resistance of angle-aligned monolayer T_d -WTe₂/monolayer H-WSe₂ heterostructure. The measurement temperature is 30 K.

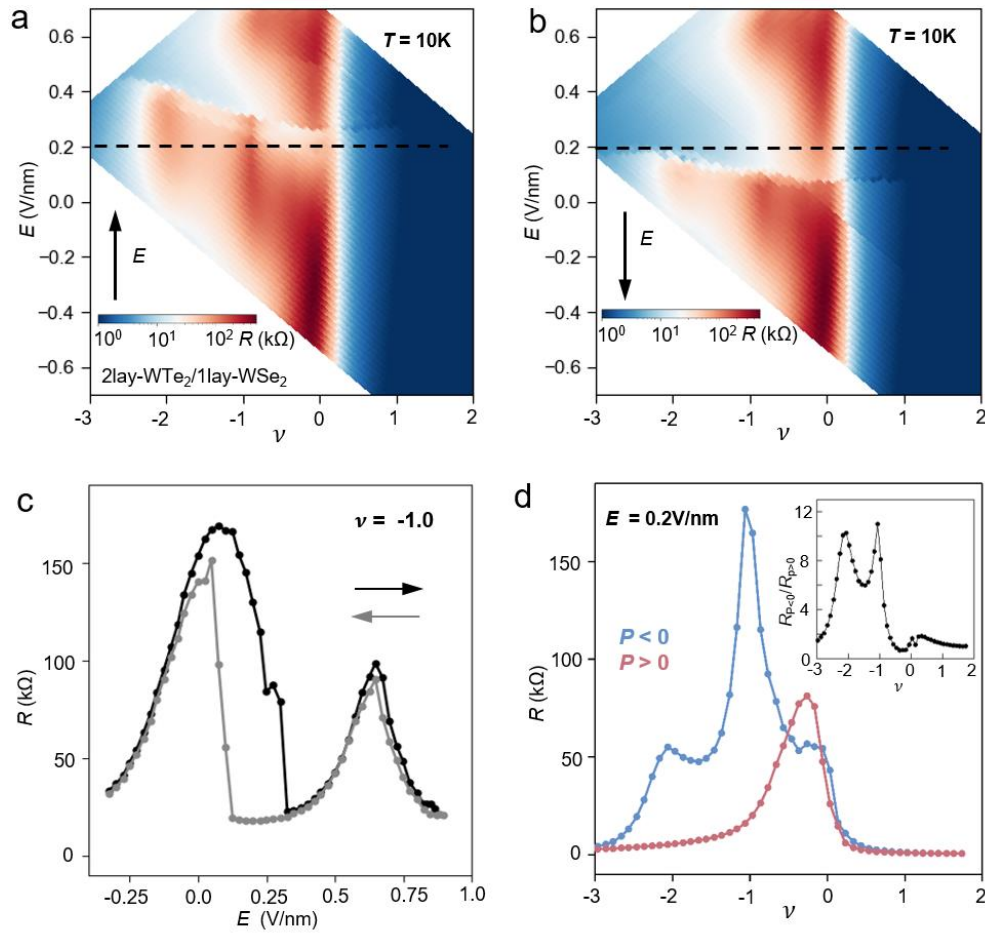


Figure 2 | Switching moiré potential by ferroelectricity. **a,b**, Electric field and filling factor dependence for the longitudinal resistance of an angle-aligned bilayer T_d - WTe_2 /monolayer H-WSe_2 heterostructure at 10 K. The black arrows label the forward (**a**) and backward (**b**) electric field scan directions. Hysteretic electric field dependence corresponding to ferroelectric switching is observed. **c**, Electric field dependence of the longitudinal resistance at $\nu = -1$. The arrows mark the field scan directions. **d**, Filling factor dependent longitudinal resistance extracted from **a** (blue) and **b** (red) at $E = 0.2$ V/nm (the black dashed lines in **a,b**). They denote the two spontaneous polarization states $P > 0$ and $P < 0$. Moiré insulating states are observed only for $P < 0$. Inset: filling factor dependent resistance on/off ratio $R_{P<0}/R_{P>0}$.

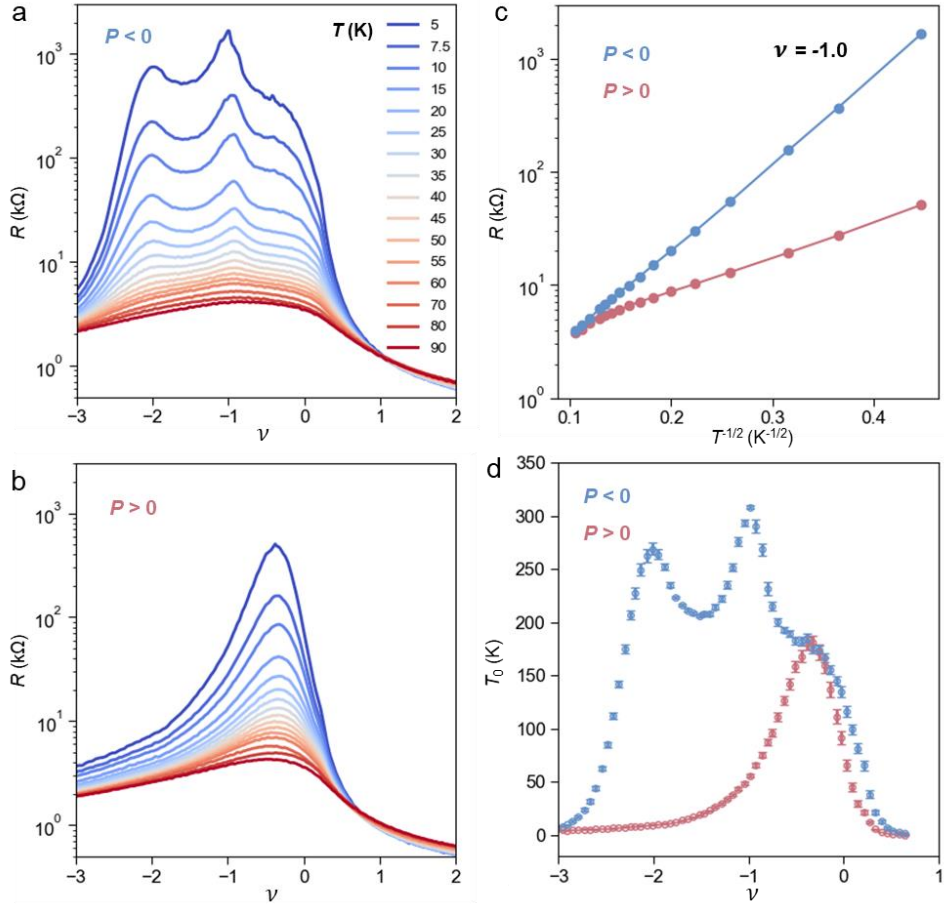


Figure 3 | Temperature dependent electrical transport. **a,b**, Filling factor dependent longitudinal resistance at varying temperatures from 5 K to 90 K for $P < 0$ (**a**) and $P > 0$ (**b**). Insulating-like behavior is observed for the entire hole-doping region in both cases. **c**, Resistance (in log scale) versus $T^{-1/2}$ at $\nu = -1$ for both $P < 0$ and $P > 0$. The linear dependence demonstrates the Efros-Shklovskii variable-range hopping. **d**, Filling factor dependence of the extracted temperature T_0 for both $P < 0$ and $P > 0$. Significant enhancements at the moiré insulating states are observed, showing the shortened localization lengths when the moiré potential is turned on.

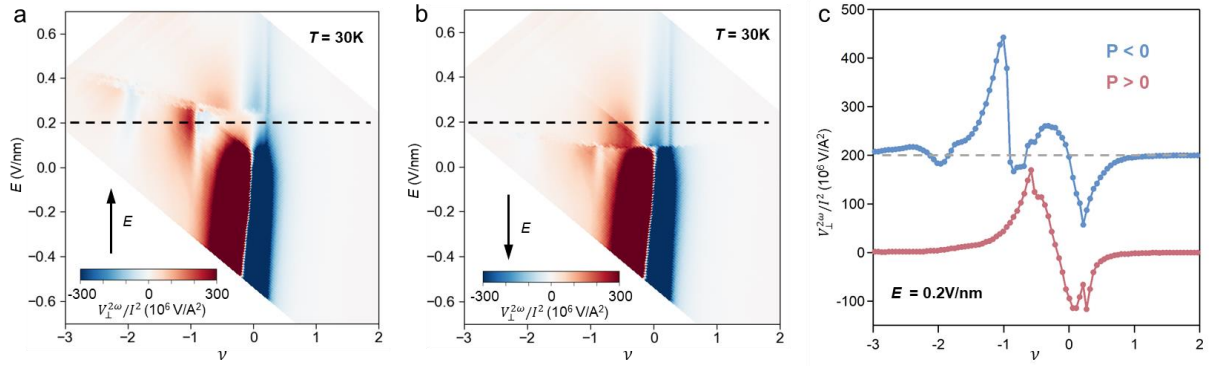
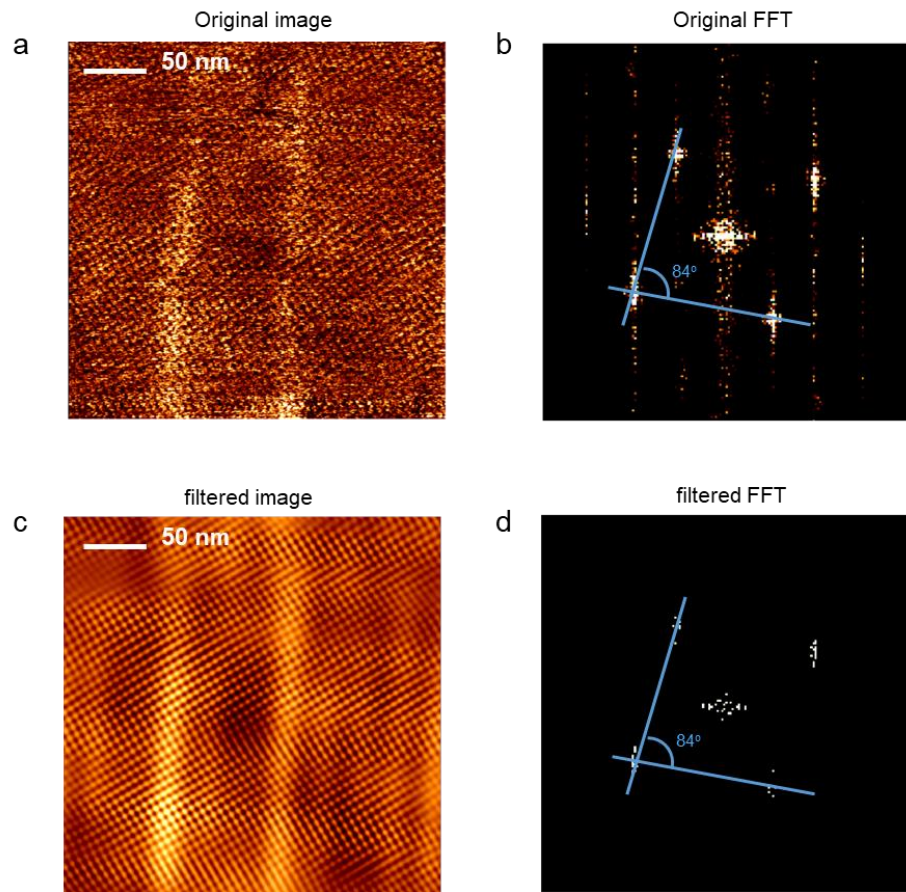
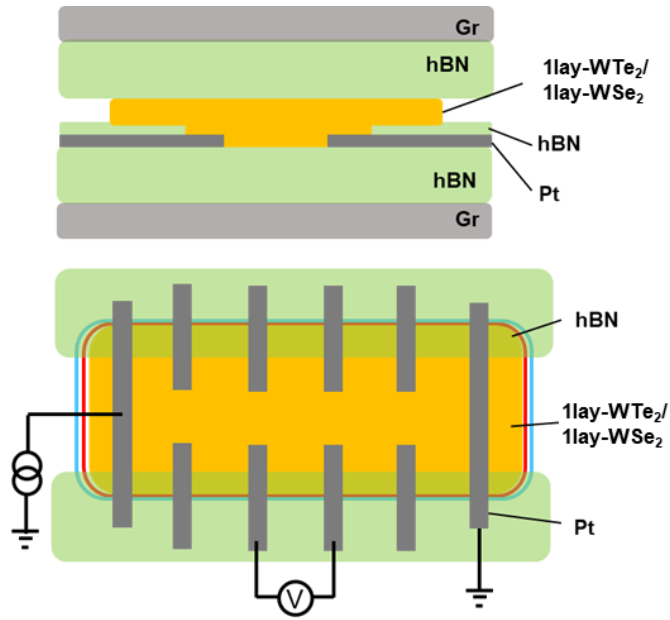


Figure 4 | Switching the nonlinear anomalous Hall transport by ferroelectricity. **a, b**, Electric field and filling factor dependent nonlinear anomalous Hall response $V_{\perp}^{2\omega}/I^2$ for the forward (**a**) and backward (**b**) electric field scan directions (black arrows). Hysteretic electric field dependence corresponding to ferroelectric switching is observed. **c**, Filling factor dependent $V_{\perp}^{2\omega}/I^2$ for $P < 0$ and $P > 0$ extracted from **a** (blue) and **b** (red), respectively, at $E = 0.2 \text{ V/nm}$ (the black dashed lines in **a, b**). The two curves are vertically displaced for clarity. The horizontal dashed line marks $V_{\perp}^{2\omega}/I^2 = 0$ for $P < 0$. Nonlinear anomalous Hall resets are observed at the moiré insulating states at $\nu = -1, -2$ only for $P < 0$.

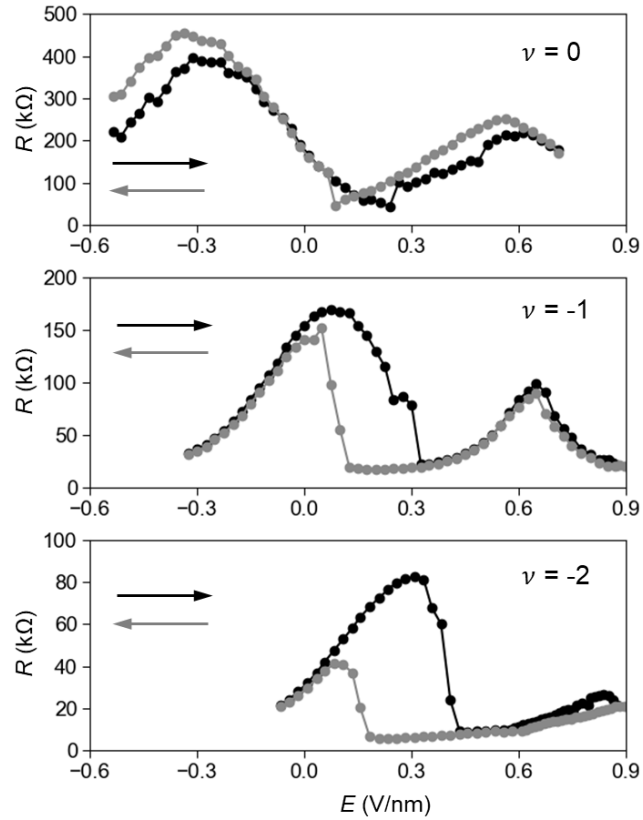
Extended Data Figures



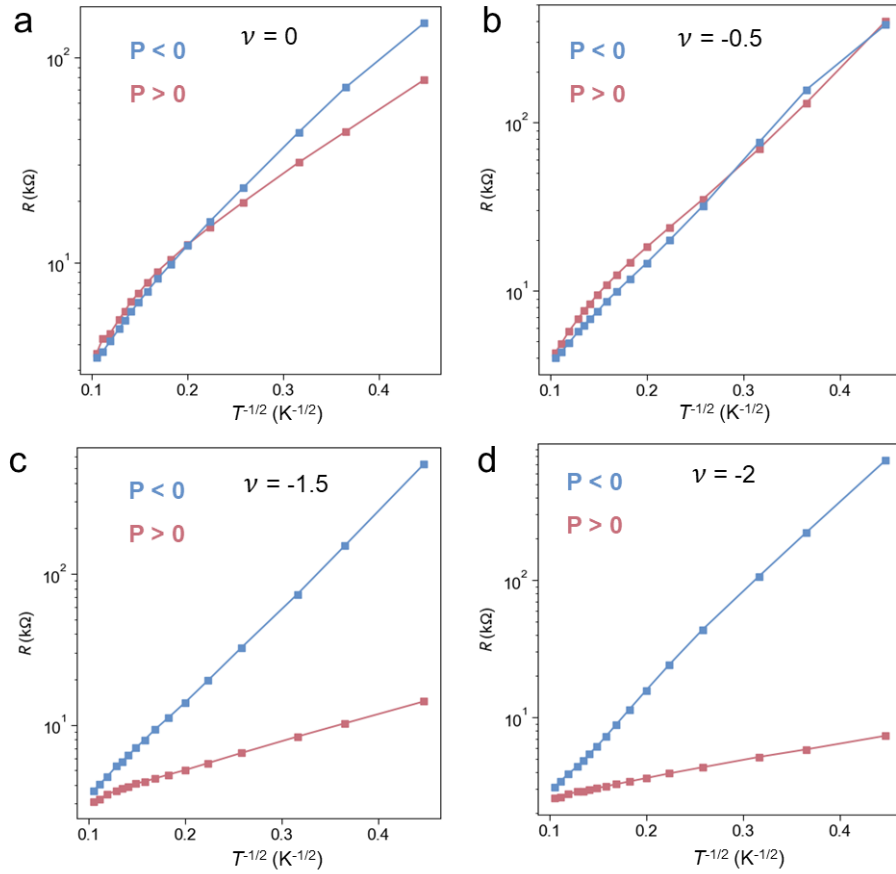
Extended Data Figure 1 | PFM images and analysis. **a**, Raw PFM image of an angle-aligned monolayer T_d - WTe_2 /monolayer H - WSe_2 heterostructure. **b**, Fourier transform of the raw image. Fourier peaks corresponding to a centered-rectangular lattice can be clearly observed. **c**, **d**, The Fourier-filtered PFM image (**c**) and the corresponding Fourier transform (**d**). A high-pass filter is applied with a threshold of 72 % of the maximum intensity.



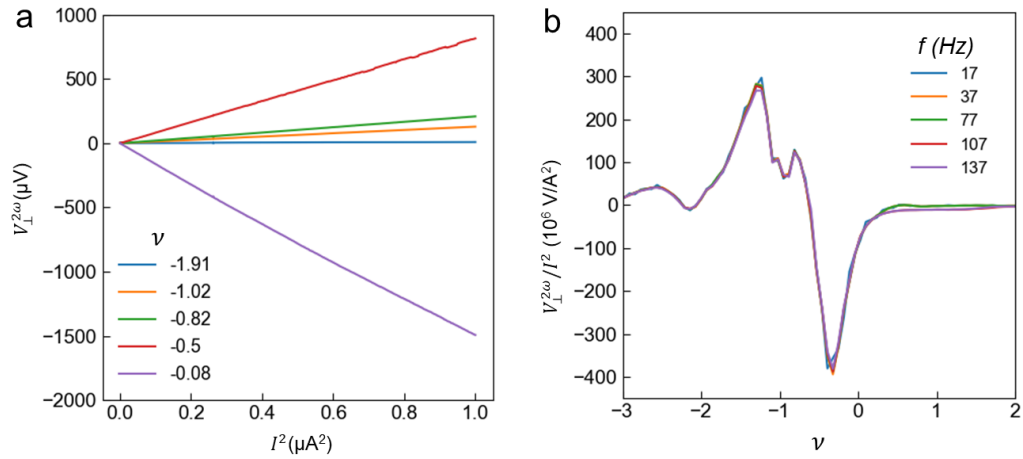
Extended Data Figure 2 | Schematics of an angle-aligned monolayer $Ta\text{-}WTe_2$ /monolayer $H\text{-}WSe_2$ Corbino device. Top: cross-section of the device. A thin hBN spacer is inserted in between the WTe_2 and the platinum (Pt) electrodes to avoid direct edge contacts. Gr stands for few-layer graphite gate electrode. Bottom: top view of the device. The blue and red lines denote the helical edge states of a quantum spin Hall insulator. The measurement configuration is also shown.



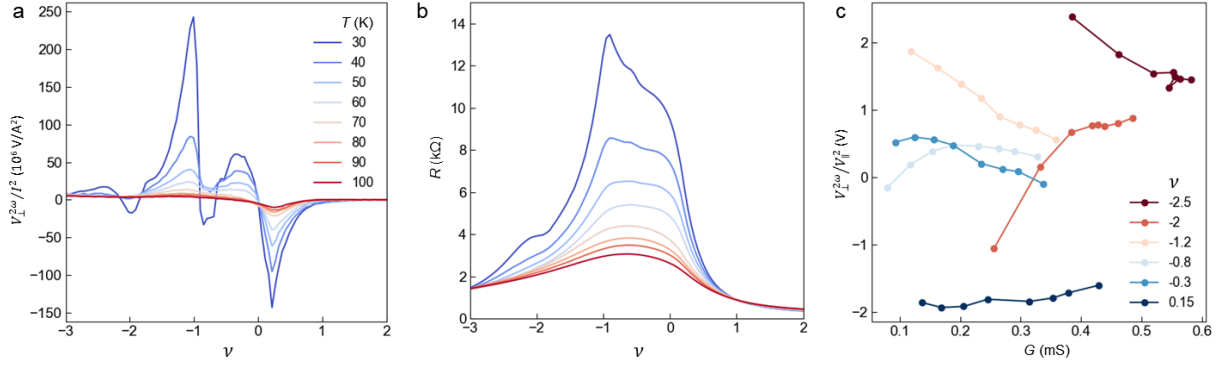
Extended Data Figure 3 | Electric field dependent resistance at selected filling factors of $\nu = 0, -1, -2$. Arrows denote the electric field scan directions. The measurement temperature is 10 K. A clear hysteresis corresponding to ferroelectric switching is observed. In addition to the ferroelectric switching, non-monotonic electric field dependence is also observed (see discussions in Methods).



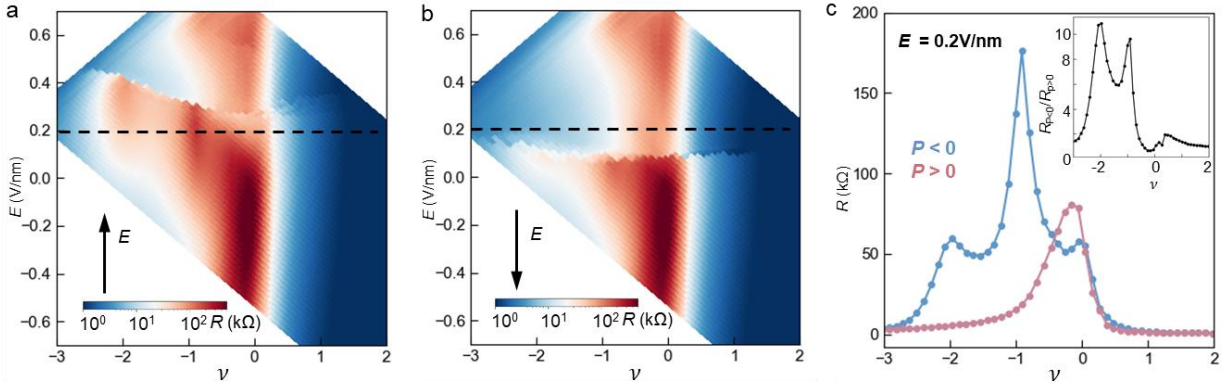
Extended Data Figure 4 | Variable-range hopping transport at different filling factors. a-d, Resistance (in log scale) versus $T^{-1/2}$ for both $P < 0$ and $P > 0$ at $\nu = 0$ (a), -0.5 (b), -1.5 (c) and -2 (d). The linear dependence demonstrates the Efros-Shklovskii variable-range hopping.



Extended Data Figure 5 | Nonlinear anomalous Hall response. a, Linear dependence of the second-harmonic Hall voltage on the bias current squared at varying filling factors. The current modulation frequency is 17 Hz. The measurement temperature is 25 K. **b**, Filling factor dependence of the nonlinear anomalous Hall response $V_{\perp}^{2\omega}/I^2$ at zero bottom gate voltage and at varying excitation frequencies of 17, 37, 77, 107, and 137 Hz. The response is independent of the excitation frequency.



Extended Data Figure 6 | Temperature dependent nonlinear anomalous Hall effect at $E = 0.2 \text{ V/nm}$ and $P < 0$. **a,b**, Filling factor dependence of $\frac{V_{\perp}^{2\omega}}{I^2}$ (**a**) and the longitudinal resistance R (**b**) at varying temperatures from 30 K to 100 K. **c**, Extracted $V_{\perp}^{2\omega}/V_{\parallel}^2$ as a function of the sample conductance G at selected moiré filling factors from -2.5 , to 0.15 . Unlike the extrinsic NAHE in the coherent metallic transport regime, in which $V_{\perp}^{2\omega}/V_{\parallel}^2 \propto G^2$ is expected and has been observed²⁵, complicated dependence of $V_{\perp}^{2\omega}/V_{\parallel}^2$ on G is observed for the variable-range hopping transport regime here. Future studies are required to better understand the NAHE in the hopping transport regime.



Extended Data Figure 7 | Transport studies along the WTe₂ crystal b-axis. **a,b**, Electric field and filling factor dependence for the longitudinal resistance of angle-aligned bilayer T_d-WTe₂/monolayer H-WSe₂ heterostructure at 10 K. The current is biased along the crystal b-axis of WTe₂. The black arrows label the forward (**a**) and backward (**b**) electric field scan directions. Hysteretic electric field dependence corresponding to ferroelectric switching is observed. **c**, Filling factor dependent longitudinal resistance extracted from **a** (blue) and **b** (red) at $E = 0.2$ V/nm (the black dashed lines in **a,b**). They denote the two spontaneous polarization states $P > 0$ and $P < 0$. Moiré insulating states are observed only for $P < 0$. Inset: filling factor dependent resistance on/off ratio $R_{P<0}/R_{P>0}$.